Journal of Magnetic Resonance 204 (2010) 56–63

Contents lists available at ScienceDirect

Journal of Magnetic Resonance

journal homepage: www.elsevier.com/locate/jmr

Heisenberg spin exchange effects of nitroxide radicals on Overhauser dynamic nuclear polarization in the low field limit at 1.5 mT

Mark D. Lingwood, Ivan A. Ivanov [1], Alissa R. Cote [2], Songi Han *

Department of Chemistry and Biochemistry, University of California, Santa Barbara, Santa Barbara, CA 93106-9510, USA

ARTICLE INFO

Article history:
Received 13 November 2009
Revised 20 January 2010
Available online 6 February 2010

Keywords:
Dynamic nuclear polarization
DNP
Hyperpolarization
Overhauser effect
Low field
NMR
Portable NMR
Portable MRI

ABSTRACT

Nuclear magnetic resonance (NMR) and magnetic resonance imaging (MRI) at very low magnetic fields (0.05–20 mT) have gained interest due to the simple and portable magnet design and newly emerging applications outside of the usual laboratory setting. A method to enhance the NMR signal is needed due to the low thermal polarization of nuclear spins at these fields; dynamic nuclear polarization (DNP) via the Overhauser effect from free radicals is an attractive option. In this report we describe a DNP-enhanced NMR system operating at a fixed field of 1.5 mT and measure ^{1}H signal enhancements of up to −350 fold during the saturation of a selected electron spin resonance (ESR) transition of dissolved nitroxide radicals. This −350 fold enhanced polarization is equivalent to what would be obtained by pre-polarization in a 0.53 T field. The ESR spectra at varying radical concentrations are indirectly found through DNP-enhanced NMR detection. Here, ESR line broadening at higher radical concentrations due to Heisenberg electron spin exchange is observed. Enhancements in the limit of maximum power are reported as a function of concentration for three ESR transitions, and are found to increase with concentration. The >300 fold ^{1}H NMR signal amplifications achievable at 1.5 mT will reduce experimental time by several orders of magnitude, permitting NMR relaxation, imaging or pulsed-field gradient diffusion experiments that are inaccessible without using the DNP effect at 1.5 mT. We demonstrate the potential benefit of such large signal amplification schemes through T_1 and T_2 relaxation measurements carried out in a much shorter time when employing DNP. Finally, we compare our results to those obtained in the earth's magnetic field and find that the signal to noise ratio (SNR) of DNP-enhanced signal at 1.5 mT is much greater than that obtained by previous studies utilizing DNP enhancement in the 0.05 mT earth's magnetic field.

1. Introduction

In recent years, nuclear magnetic resonance (NMR) and magnetic resonance imaging (MRI) at very low magnetic fields have gained interest due to the ability to use portable and often simple magnet designs. While the magnetic field inhomogeneities present in such magnets prevent spectroscopy and chemical shift resolution, a wide array of other experiments are still feasible, such as relaxation measurements [1,2], diffusion experiments [3–5], 2D NMR [6] and MRI acquisition [7]. Portable magnetic resonance has found a diverse range of applications, including well-logging [8], food quality control [9], the study of intact plants [10], materials [1,11] and cultural artifacts [12,13].

At very low magnetic fields it is necessary to use some form of signal enhancement to overcome the low thermal polarization of the nuclei. The first of two common methods is prepolarization [3,5,14], where the sample is placed in a higher magnetic field until reaching thermal polarization then returned to the low field for signal acquisition. Very inhomogeneous polarization fields can be used and either permanently placed around the sample (prepolarization coils) or installed as a separate magnet (sample shuttling). Prepolarization has the disadvantage of potentially complicating magnet design but more importantly limits the type of samples that can be used, because the sample needs to have a longitudinal relaxation time T_1 long enough for the prepolarization to last through the time to switch off the prepolarization coil (40–150 ms [15–18]) or physically shuttle the sample. The second signal enhancement method is hyperpolarization, where the higher polarization from a second group of spins is transferred to the target nuclei for detection. While methods such as parahydrogen-induced polarization (PHIP) [19,20] or dissolution dynamic nuclear polarization [21] could be used at low fields, it is technologically and experimentally simpler to dissolve a stable radical in the

* Corresponding author. Fax: +1 805 893 4120.
E-mail address: songi@chem.ucsb.edu (S. Han).
[1] Present address: Department of Chemistry and Biochemistry, University of California, Los Angeles, CA 90095, USA.
[2] Present address: Materials Science and Engineering, University of Illinois, Urbana, IL 61801, USA.

1090-7807/$ - see front matter © 2010 Elsevier Inc. All rights reserved.
doi:10.1016/j.jmr.2010.01.015

sample and utilize liquid-state Overhauser dynamic nuclear polarization (DNP). Here, we focus on the utilization of the Overhauser DNP effect for signal amplification because it can give higher polarization using simple and light-weight hardware and provides the possibility of signal accumulation with faster repetition delays than are feasible with field cycling or sample shuttling. Recent applications of Overhauser DNP at low fields have included MRI contrast [22–24] oximetry [25–27] and pH determination [28], monitoring of free-radical reaction products [29], magnetometry at low magnetic fields [30] and two-dimensional spectroscopy [17].

Previously, Overhauser DNP has been described using the earth's magnetic field (0.05 mT [17]) and fields between 1 and 9 mT [16,18,31–33]). All of these experiments were performed with field-cycling DNP [32,34], where the field is cycled to a polarization field for electron saturation then returned to a lower or higher value for NMR detection. One advantage of this method is that the radio frequency (RF) saturation coil can remain tuned at a given frequency, but similar to prepolarization a more complex setup is required, signal accumulation takes longer and the application to samples with short T_1 is limited. A few studies have been performed with a constant magnetic field [35,36] but have employed low radical concentrations and focused on theoretical aspects of the Overhauser DNP effect. In this paper we investigate the NMR signal enhancement through Overhauser DNP at a fixed magnetic field and describe the optimal radical concentration and frequency of electron spin resonance (ESR) saturation for maximum signal amplification effects at 1.5 mT, thus providing guidelines for carrying out NMR relaxation, diffusion and imaging experiments using hyperpolarized signal.

2. Theory

To perform DNP via the Overhauser effect, an electron transition of the radical is saturated with on-resonant radiation. This non-equilibrium population distribution is then transferred to nuclear spins that experience a rapidly modulated dipolar field from the electron spin due to molecular diffusion. We begin by describing the ESR transitions at low magnetic fields then relate these to the DNP factors of the nuclei, for the purpose of showing where the theory breaks down at higher radical concentrations. More detailed accounts of the theory for both ^{14}N and ^{15}N nitroxide radicals can be found in the literature [16,18,32,37].

Most experiments are performed with ^{14}N nitroxide radicals, where the unpaired electron spin S = 1/2 is coupled to a nitrogen nuclear spin K = 1 by the hyperfine constant A. The time-independent Hamiltonian of the nitroxide radical in an external magnetic field B_0 is described in angular frequency units by

$$\mathscr{H} = -\gamma_S \boldsymbol{B}_0 \cdot \boldsymbol{S} - \gamma_K \boldsymbol{B}_0 \cdot \boldsymbol{K} + A\boldsymbol{K} \cdot \boldsymbol{S} \tag{1}$$

where γ_S and γ_K are the gyromagnetic ratios of spins S and K. In a high magnetic field, spins S and K are coupled only through the hyperfine interaction and lead to the familiar six wavefunctions of the nitroxide system, labeled here in order of decreasing energy with $|1\rangle = |m_S, m_K\rangle = |1/2, 1\rangle, |2\rangle = |1/2, 0\rangle, |3\rangle = |1/2, -1\rangle, |4\rangle = |-1/2, -1\rangle, |5\rangle = |-1/2, 0\rangle$ and $|6\rangle = |-1/2, 1\rangle$. In low magnetic fields, however, spins S and K are strongly coupled and the wavefunctions are superpositions of the high field states:

$$\begin{aligned}
|1'\rangle &= |1\rangle \\
|2'\rangle &= C_1|2\rangle + C_2|6\rangle \\
|3'\rangle &= C_4|3\rangle + C_3|5\rangle \\
|4'\rangle &= |4\rangle \\
|5'\rangle &= C_4|5\rangle - C_3|3\rangle \\
|6'\rangle &= C_1|6\rangle - C_2|2\rangle
\end{aligned} \tag{2}$$

The squared constants are given by

$$\begin{aligned}
(C_1)^2 &= \frac{1}{2}\left(1 + \frac{-2\omega_S + A}{\sqrt{9A^2 - 4\omega_S A + 4\omega_S^2}}\right) \\
(C_2)^2 &= \frac{1}{2}\left(1 - \frac{-2\omega_S + A}{\sqrt{9A^2 - 4\omega_S A + 4\omega_S^2}}\right) \\
(C_3)^2 &= \frac{1}{2}\left(1 + \frac{2\omega_S + A}{\sqrt{9A^2 + 4\omega_S A + 4\omega_S^2}}\right) \\
(C_4)^2 &= \frac{1}{2}\left(1 - \frac{2\omega_S + A}{\sqrt{9A^2 + 4\omega_S A + 4\omega_S^2}}\right)
\end{aligned} \tag{3}$$

where ω_S is the electron Larmor frequency. In Eq. (3) the nitrogen Larmor frequency is neglected and while the equations give the same result described by Guiberteau and Grucker [16] the simpler formalism of Fedin et al. is used [38]. At high magnetic fields C_2 and C_3 converge to zero. The energy level of each state is given directly by the Breit–Rabi equations [39] and is well described by other authors [34,37]; a plot of the energy levels is presented in Fig. 1.

At low magnetic fields ten transitions are possible, as opposed to three that are allowed at high magnetic fields. The eight transitions that are induced by RF radiation perpendicular to B_0 are known as π transitions: T_{12}, T_{16}, T_{23}, T_{25}, T_{34}, T_{36}, T_{45} and T_{56}. The other two transitions, T_{26} and T_{35}, are called σ transitions and are induced by RF parallel to B_0. The transition frequencies as a function of magnetic field are shown in Fig. 2. Note that at zero magnetic field or in the earth's magnetic field all transitions occur with a frequency of 3/2 A, around 70 MHz. The transition probabilities are given by the following [16,32],

$$\begin{aligned}
W_{12} &= (c/4)(C_2)^2(\sin\phi)^2 \\
W_{16} &= (c/4)(C_1)^2(\sin\phi)^2 \\
W_{23} &= (c/4)(C_1C_3)^2(\sin\phi)^2 \\
W_{25} &= (c/4)(C_1C_4)^2(\sin\phi)^2 \\
W_{34} &= (c/4)(C_4)^2(\sin\phi)^2 \\
W_{36} &= (c/4)(C_2C_3)^2(\sin\phi)^2 \\
W_{45} &= (c/4)(C_3)^2(\sin\phi)^2 \\
W_{56} &= (c/4)(C_2C_4)^2(\sin\phi)^2 \\
W_{26} &= c(C_1C_2)^2(\cos\phi)^2 \\
W_{35} &= c(C_3C_4)^2(\cos\phi)^2
\end{aligned} \tag{4}$$

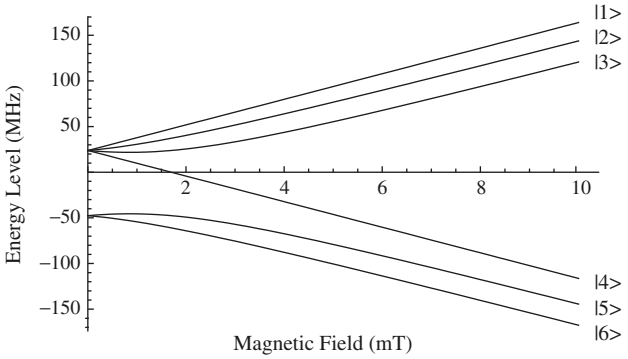

Fig. 1. Electron energy levels for the coupled two-spin system of a ^{14}N nitroxide radical as a function of magnetic field strength, calculated with a hyperfine coupling constant of A = 47.6 MHz. The energy axis is given in megahertz corresponding to the ESR frequency of a given energy difference.

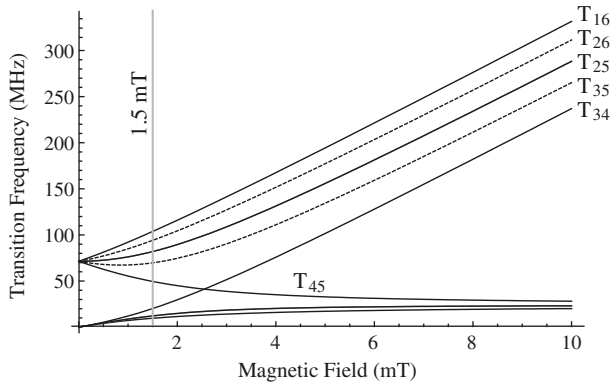

Fig. 2. Transition frequencies for the ^{14}N nitroxide system as a function of magnetic field strength. The solid lines represent π transitions, while the dashed lines depict σ transitions. While the σ transition frequency continually increases, the transition probability decreases with increasing field. The vertical line represents the fixed magnetic field strength used in this experiment, 1.5 mT.

where c is a normalization constant such that the sum of all transition probabilities is equal to one for each B_0 value and φ is the angle of the RF excitation field with respect to B_0. Since C_2 and C_3 converge to zero as magnetic field increases, only the T_{16}, T_{25} and T_{34} transitions have a non-zero probability at high magnetic fields.

In a ^{1}H DNP experiment the nitroxide radical is also coupled to the protons of the solvent. The amount of ^{1}H signal enhancement upon saturation of the ESR transitions is known as the DNP factor (DNPF), and is defined as [16]

$$\mathrm{DNPF} = \frac{\langle I_Z\rangle}{I_0} = 1 - \rho f s^* \left(\frac{\langle S_Z\rangle - S_0}{I_0}\right) \tag{5}$$

The polarization of spins I and S after ESR saturation are denoted I_Z and S_Z while the polarization of the spins at thermal equilibrium are I_0 and S_0. The coupling factor, ρ, gives the degree of coupling between the electron and proton and can range from −1 (pure scalar coupling) to 0.5 (pure dipolar coupling). The coupling factor for ^{1}H at low magnetic fields is very close to 0.5 due to almost exclusive dipolar coupling [40] and low field values [41]. The leakage factor f describes how much of the nuclear spin relaxation is due to the radical and ranges from 0 to 1, and is easily measured with the relation $f = 1 - T_1/T_{10}$, where T_1 and T_{10} are the longitudinal relaxation rate constants of the nucleus with and without radicals, respectively. The leakage factor approaches 1 as concentration increases. The saturation parameter s^* gives the amount of saturation of the individual ESR transition under study and lies between 0 and 1 if there is no mixing of the individual hyperfine lines. However, as will be described later, if mixing of hyperfine lines occurs the values of s^* can effectively become much larger than 1. Here, the saturation factor is labeled s^* to illustrate the difference from the saturation factor as conventionally used in DNP theory, s, which gives the saturation of the whole electron system across all hyperfine lines [41]. The parameter s^* is an addition used only to describe the low field system, whereas the high field form of Eq. (5) is normally written as:

$$\mathrm{DNPF} = 1 - \rho f\left(\frac{\langle S_Z\rangle - S_0}{I_0}\right) = 1 - \rho f\left(\frac{S_0 - \langle S_Z\rangle}{S_0}\right)\frac{|\gamma_S|}{\gamma_I} = 1 - \rho f s\left(\frac{|\gamma_S|}{\gamma_I}\right) \tag{6}$$

The difference between $\langle S_Z\rangle$ and S_0 is calculated with

$$\langle S_Z\rangle - S_0 = \sum_i \langle i|S_Z|i\rangle(n_i - n_i^0) \tag{7}$$

where i represents each state $|1'\rangle$ through $|6'\rangle$ and n_i^0 and n_i are the populations of state i before and after saturation of the ESR transition, respectively. The thermal polarization of each state, n_i^0, can be easily calculated with the high-temperature approximation of Boltzmann's law:

$$n_i^0 = \frac{1}{(2S+1)(2K+1)}\left(1 - \frac{E_i}{kT}\right) \tag{8}$$

Combining Eqs. (2), (5), and (7) with the use of $\Delta n_i = n_i - n_i^0$ gives the DNP factor for the saturation of the transition T_{ij}

$$\mathrm{DNPF}_{ij} = 1 - \frac{\rho f s^*}{2I_0}[(\Delta n_1 - \Delta n_4) + (\Delta n_2 - \Delta n_6)(1 - 2(C_2)^2) + (\Delta n_3 - \Delta n_5)(1 - 2(C_3)^2)] \tag{9}$$

Guiberteau and Grucker made the following two assumptions [16]

$$n_i = n_j = \frac{n_i^0 + n_j^0}{2} \tag{10}$$

$$\Delta n_k = 0 \quad \forall \quad k \neq i,j \tag{11}$$

in order to calculate the DNP factors as the following,

$$\begin{aligned}
\mathrm{DNPF}_{12} &= -d(E_1 - E_2)(C_2)^2 W_{12}\\
\mathrm{DNPF}_{16} &= -d(E_1 - E_6)(C_1)^2 W_{16}\\
\mathrm{DNPF}_{23} &= -d(E_2 - E_3)((C_3)^2 - (C_2)^2) W_{23}\\
\mathrm{DNPF}_{25} &= -d(E_2 - E_5)((C_1)^2 - (C_3)^2) W_{25}\\
\mathrm{DNPF}_{34} &= -d(E_3 - E_4)(C_4)^2 W_{34}\\
\mathrm{DNPF}_{36} &= -d(E_3 - E_6)((C_1)^2 - (C_3)^2) W_{36}\\
\mathrm{DNPF}_{45} &= +d(E_4 - E_5)(C_3)^2 W_{45}\\
\mathrm{DNPF}_{56} &= -d(E_5 - E_6)((C_3)^2 - (C_2)^2) W_{56}\\
\mathrm{DNPF}_{26} &= -d(E_2 - E_6)(1 - 2(C_2)^2) W_{26}\\
\mathrm{DNPF}_{35} &= -d(E_3 - E_5)(1 - 2(C_3)^2) W_{35}
\end{aligned} \tag{12}$$

where $d = \rho f s^*/12kTI_0$.

The preceding equations are valid for low radical concentrations, but the assumption in Eq. (11) is no longer true if Heisenberg electron spin exchange mixes the hyperfine states of the nitroxide radical. Heisenberg spin exchange is a process where two radicals with opposite electron spins exchange during a molecular collision leading to the mixing of hyperfine states; with regards to DNP this spin exchange mixing is significant above 0.5 mM radical concentration [42]. Therefore, the assumption that no other states k experience a population change during the saturation of the i j transition is not valid if states i or j participate in Heisenberg spin exchange, as the saturation of i and j will affect the population of other states. To compensate for this invalid assumption, the parameter s^* has been added to the equations in this paper.

Heisenberg spin exchange also plays a key role in broadening ESR lines, in fact the first observation of spin exchange was made through ESR linewidths [43]. At radical concentrations higher than ~3 mM, spin exchange broadening is the dominant mechanism and the linewidth is given by [44]

$$\Gamma = \Gamma_0 + u\frac{k[\mathrm{R}]}{|\gamma_S|} \tag{13}$$

where Γ is the absorption linewidth, Γ_0 is the theoretical linewidth at zero concentration, k is the electron exchange rate and [R] is the concentration of radicals. The constant u relates to the probability of an exchange event occurring between two radicals with different hyperfine states, and $u = 2/3$ at high magnetic fields. In the low field case u is likely to be much closer to 1.

The result of the invalid assumption in Eq. (11) on the DNP factors is unclear. At high magnetic fields, the addition of Heisenberg spin exchange has been fully described by Bates and Drozdoski

[45,46], where it primarily effects the saturation factor. The saturation factor used in the high field case, s, relates to the saturation of the whole electron system (Eq. (6)). The maximum saturation s at low radical concentrations is $s = 1/n$ where n is the number of hyperfine lines in the spectrum (3 for ^{14}N nitroxides at high field) because there is no mixing of the individual hyperfine lines. At high radical concentrations (10–20 mM) with the addition of exchange effects, the saturation factor can reach $s \to 1$. However, in the low field formalism, s^* only depends on ESR saturation power and will approach 1 at low radical concentrations in the absence of electron spin exchange, since the parameter relates to the saturation of the individual hyperfine transition. The addition of Heisenberg spin exchange at high radical concentrations would affect more Δn_i terms in Eq. (9) than the two from the saturated transition, and if it was known how the other Δn_i terms were affected new DNP factors could be calculated. Since the change of other Δn_i terms with spin exchange is unknown, the effect of spin exchange can be compensated for by increasing the saturation factor s^* to values higher than 1, up to a maximum value of ~10.

The expansion of the Bates model [45] for the complete description of the transitions at 1.5 mT is an intractable problem, as it requires the solution of a system of 40 equations even with assumptions used in the high field case. Instead, in this paper we account for the effects of exchange on various transitions by employing values of s^* greater than 1 and describe the observed spectra and enhancements with currently available theory.

3. Results

Using the homebuilt 1.5 mT electromagnet and DNP-NMR system, saturating the T_{16} transition gave ^{1}H NMR signal enhancements of −350 over thermal polarization for the solvent water protons in a 20 mM solution of the free radical 4-amino-2,2,6,6-tetramethylpiperidine-1-oxyl (4-amino-TEMPO). This was the highest observed enhancement, although it was only slightly larger than 10 mM solutions of 4-amino-TEMPO. Enhanced signal was clearly visible in a single acquisition, while unenhanced signal required between 100 and 1000 scans.

3.1. Frequency swept DNP experiment

By recording the ^{1}H NMR signal enhancement at a constant field as a function of ESR irradiation frequency, the shape of the ESR spectrum can be reproduced and the various transitions observed. The frequency swept DNP spectra are shown in Fig. 3 with 4-amino-TEMPO radical concentrations of 1, 15 and 40 mM. The 1 mM spectrum, Fig. 3A, shows the contribution of both π and σ transitions with ESR saturation both perpendicular and parallel to B_0. The only σ transition observed was T_{26}, the T_{35} transition occurs at 69.9 MHz but was not seen due a slightly lower transition probability. Fig. 3B and C show the spectra for 15 and 40 mM 4-amino-TEMPO concentrations, where significant line broadening due to Heisenberg electron spin exchange is visible. Due to overlapping π and σ resonances and B_1 inhomogeneity, the σ resonances were not reliably observed at higher radical concentrations and are not reported. Care was taken to deliver the same RF power to the sample for each frequency, but was experimentally difficult to ensure due to variances in probe tuning and amplifier output at each frequency. This was taken into account when fitting the spectra, as discussed in the next paragraph. As a reference the B_1 output of the ESR saturation coil was measured as a function of frequency and is shown in Fig. 3D.

The theoretical spectrum (solid line) in Fig. 3A was created by placing Lorentzian absorption lineshapes at each transition frequency, with the exclusion of the T_{35} resonance. The amplitude

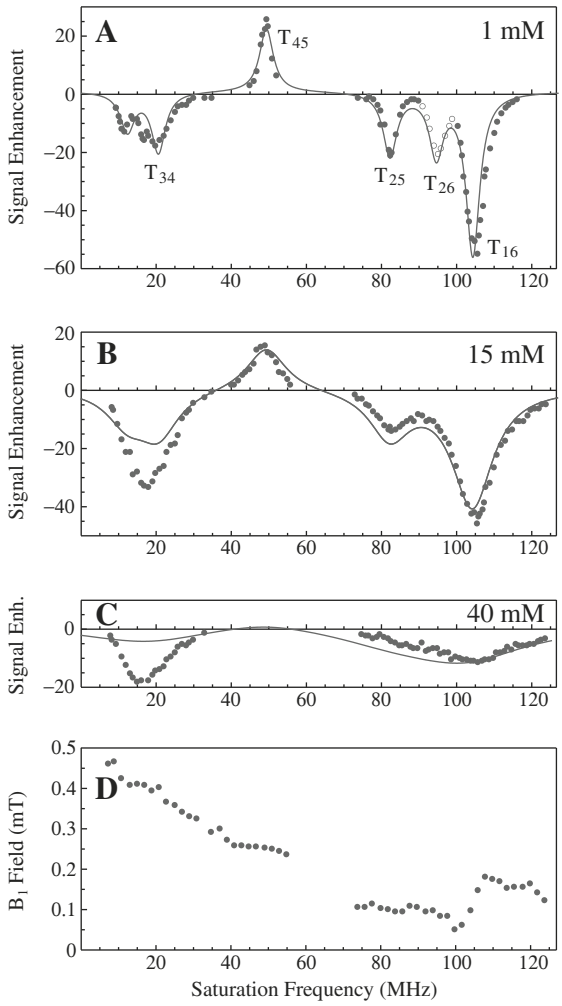

Fig. 3. (A) DNP-enhanced NMR signal as a function of ESR irradiation frequency at a constant field of 1.5 mT, with a 4-amino-TEMPO concentration of 1 mM. Selected transitions are labeled. The filled circles represent data taken with ESR saturation perpendicular to B_0 for the observation of π transitions while the open circles used ESR saturation parallel to B_0 to observe σ transitions. The solid trace is a theoretical spectrum calculated from the DNP factors and transition frequencies; details can be found in the text. Panels (B) and (C) also show DNP-enhanced NMR signal as a function of frequency at 1.5 mT, with radical concentrations of 15 and 40 mM, respectively. The solid trace in both (B) and (C) was calculated similarly to (A) but with the addition of line broadening due to Heisenberg electron exchange. Panel (D) gives the B_1 output of the coil used for ESR irradiation as a function of frequency, measured with a pickup coil in place of the sample connected to an oscilloscope.

of the Lorentzians was set by the corresponding DNP factors in Eq. (12), which depended on f and s^* while ρ was assumed to be 0.5. The leakage factor of $f = 0.49$ was measured through separate experiments and used in the calculation. The data from each peak was fit separately to find the saturation factor s^*, half-linewidth at half the maximum height and exact magnetic field. The theoretical spectrum in Fig. 3A was then generated by using each peak's different saturation factor s^* and the average fit values for half-linewidth of 2.2 MHz and magnetic field of 1.5218 mT. The half-linewidth of 2.2 MHz corresponds to an electron $T_2 = 450$ ns assuming exclusively T_2 broadening.

The saturation factors (s^*) varied between 0.77 and 16.4, and are greater than 1 due to electron spin exchange as discussed in the theory section. The fit values of s^* for each peak are given in Table 1. Even though the linewidths at 1 mM radical concentration are not affected by Heisenberg spin exchange, the hyperfine states are still mixed resulting in an increase of DNP efficiency and s^* values larger than 1. As seen in Fig. 3D, the B_1 field generated by the

Table 1
The transition frequencies at 1.5218 mT and s^* parameters determined by fitting each peak, which are used for the theoretical spectra in Fig. 3. All low field transitions are included except T_{35}, which was not observed.

Transition	Frequency (MHz)	1 mM s^*	15 mM s^*	40 mM s^*
T_{12}	9.73	7.26	2.69	0.54
T_{23}	12.34	16.4	6.07	1.21
T_{56}	12.34	16.4	6.07	1.21
T_{34}	20.58	3.05	1.13	0.23
T_{45}	49.33	3.69	1.37	0.27
T_{25}	82.25	1.16	0.43	0.086
T_{36}	82.25	1.16	0.43	0.086
T_{26}	94.59	0.77	–	–
T_{16}	104.3	0.87	0.32	0.064

ESR saturation coil increases at lower frequencies, which should give higher saturation as the frequency decreases. This trend was observed, as the s^* fit values are higher for the lower frequency peaks, as shown in Table 1. The variance of the B_1 field with frequency, even over the range of a single ESR peak, will contribute to the error in our theoretical spectrum, thus the variation of the s^* parameter for each peak is an approximation that gives a sufficient theoretical spectrum. Interestingly, the s^* values for the low-frequency transitions T_{23} and T_{56} are higher than the expected maximum $s^* = 10$. The cause for this discrepancy is unclear, but it is likely that the quality of the fit is not optimal in the relatively noisy and crowded low-frequency part of the spectrum.

For the 15 mM radical concentration (Fig. 3B), the theoretical spectrum used the same parameters as Fig. 3A, except with the measured leakage factor for 15 mM of $f = 0.95$, the exclusion of the T_{26} transition, and the addition of exchange broadening in the linewidth through Eq. (13). A half-linewidth of 6.59 MHz was used, and the saturation factor of each peak was reduced by a common factor to account for the decreased saturation of broader ESR lines. An exchange rate of $0.71 \times 10^9\ M^{-1}\ s^{-1}$ gave the best fit at 1.5 mT, which is one third of the value as measured at 0.35 T. The plot in Fig. 3C (40 mM) was fit in the same manner, with $f = 1$ and an exchange broadened linewidth of 18.5 MHz, which are both due to increased radical concentration. The region between 5 and 30 MHz shows more enhancement than expected, which is most likely related to the large s^* values for these peaks in the 1 mM spectrum. This behavior could be due to the large number of transitions being saturated at each point, as the T_{12}, T_{23}, T_{34} and T_{56} are all very close in frequency.

3.2. Maximum enhancement measurements

The enhancement in the limit of maximum power, E_{max}, was measured as a function of radical concentration for the π transitions T_{16} and T_{25} and the σ transition T_{26} and is presented in Fig. 4. The E_{max} is determined by recording enhancement as a function of saturating RF power then extrapolating to infinite power, and is a useful measure of enhancement because it is reproducible across samples and systems. E_{max} is equivalent to Eqs. (5) and (9) when s^* reaches its highest possible value, and is dependent on radical concentration through the concentration dependence of the leakage factor, f, and the increase of s^* due to Heisenberg spin exchange. Fig. 4A shows that enhancement initially increases with concentration then reaches a constant value, similar to what is seen in higher fields [42]. This behavior is mainly due to the leakage factor increasing towards $f = 1$, but also partly due to s^* increasing with concentration. At high concentration, the enhancement should reach the value of the DNP factor in Eq. (12) with s^* at its maximum value. At high radical concentrations of 20 mM, the E_{max} of T_{16} corresponds to $s^* \approx 4$, the E_{max} of T_{25} corresponds to $s^* \approx 5.5$ and the E_{max} of T_{26} corresponds to $s^* \approx 1$. Since the effects of electron spin exchange are added into the current theory by increasing the saturation factor s^*, this causes s^* to be greater than one for higher radical concentrations. The behavior of the T_{26} transition is distinctive in that the E_{max} initially increases then decreases to a constant value as concentration rises. This might be due to some behavior unique to σ transitions, such as a decrease of s^* or increased broadening with concentration.

3.3. T_1 and T_2 measurements

To illustrate the utility of DNP-enhanced NMR signal in a portable, low field system, T_1 saturation-recovery measurements of

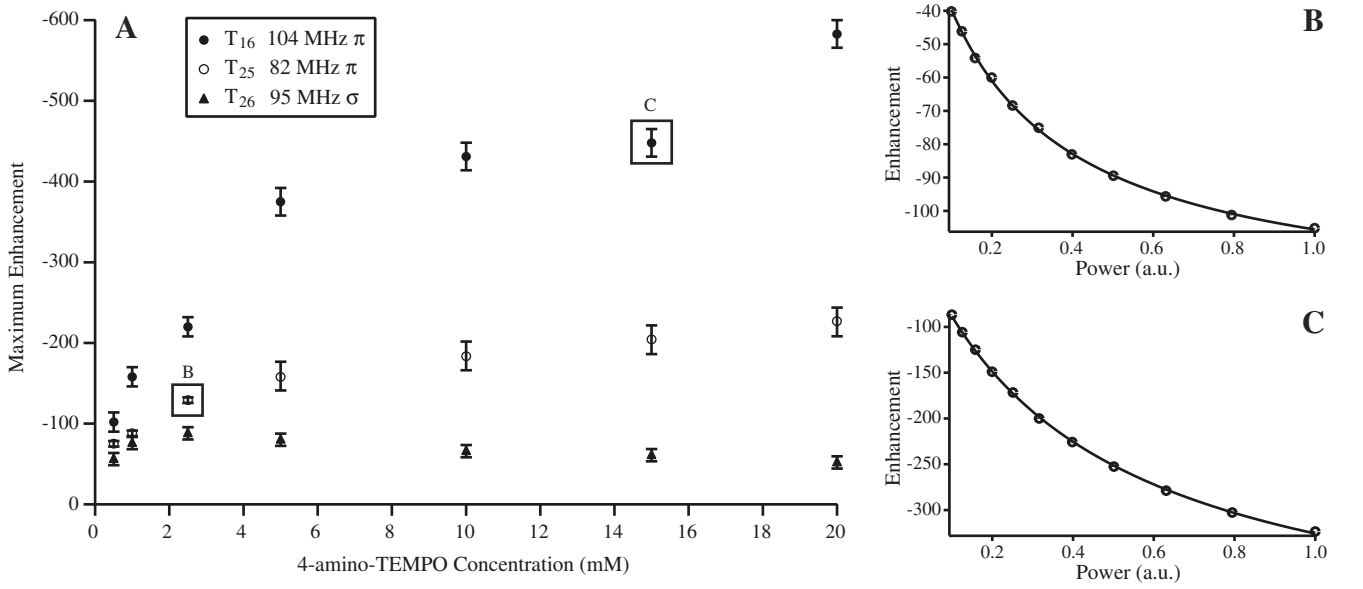

Fig. 4. Enhancement in the limit of maximum power (E_{max}) measurements at 1.5 mT. (A) E_{max} of the T_{16}, T_{25} and T_{26} transitions as a function of 4-amino-TEMPO concentration, with the y-axis inverted. The T_{16} and T_{25} values were obtained with ESR saturation perpendicular to B_0, while T_{26} was measured with ESR saturation parallel B_0. Panels (B) and (C) show the individual measurements for T_{25} at 2.5 mM and T_{16} at 15 mM, respectively. The enhancement is recorded as power is increased then extrapolated to maximum power to determine E_{max}, as detailed in the experimental section.

20 mM 4-amino-TEMPO were taken with and without the aid of DNP. The T_{16} transition was saturated with 104 MHz irradiation, because this frequency gave the highest observed enhancement (−350) and E_{max} (−583) out of all transitions studied. The result in Fig. 5A was obtained with an experimental time of 30 s employing DNP, while the result in Fig. 5B used only thermally polarized signal with an experimental time of 1 h. The T_1 values are in good agreement with T_1 = 106 ms. This nicely illustrates the convenience of using the DNP effect at low fields. Also, a DNP-enhanced measurement of transverse relaxation time, T_2, was performed with a total experimental time of 30 s and yielded a value of T_2 = 78 ms (Fig. 5C). The T_2 measurements could not be carried out using thermal polarization due to low signal and high noise figures at 1.5 mT. In these experiments, we saw a reduction of experimental time by a factor of 120, but for other types of experiments such as pulsed-field gradient diffusion measurements or MRI the time savings will be much larger. The same signal to noise ratio (SNR) found in the −350 fold enhanced spectrum would require $350^2 = 1.2 \times 10^5$ transients to achieve the same signal amplitude without enhancements at the same detection field of 1.5 mT, and thus the use of the DNP effect could reduce experimental time by five orders of magnitude. A wide range of NMR relaxation, diffusion and imaging experiments on sample systems that are not feasible at 1.5 mT will become amenable when DNP is utilized.

4. Conclusion

DNP-enhanced NMR is an effective way to increase signal in very low magnetic fields. At 1.5 mT we observed signal enhancements of −350 with 104 MHz ESR saturation of the T_{16} transition. This amplification factor could also be achieved by employing a prepolarization field of 0.53 T. Such fields cannot be easily created by fast switching of portable electromagnetic coils, but are feasible using specialized, state of the art, Halbach type permanent magnets. However, the use of permanent Halbach magnets would require physical sample shuttling over a relatively large distance of ~40 cm, and thus is not a feasible approach for most ^{1}H NMR samples with relatively short T_1 relaxation times. Also, physical sample shuttling is not feasible for imaging and diffusion measurements using pulsed-field gradient NMR approaches due to distortions of sample position, shape, packing and/or dynamics. The effect of radical concentration on the DNP detected ESR spectrum was demonstrated, with the observation of significant line broadening due to Heisenberg electron spin exchange at higher radical concentrations. Maximum enhancements were shown to increase with concentration, as expected from the concentration dependent characteristics of the leakage factor and saturation factor. T_1 and T_2 experiments were performed to demonstrate the utility of DNP for measurements in a low field, portable magnet, when sample and signal amplitude is limited. Experiments that may particularly benefit from such prospects include multi- dimensional relaxation, pulsed-field gradient diffusion or imaging experiments.

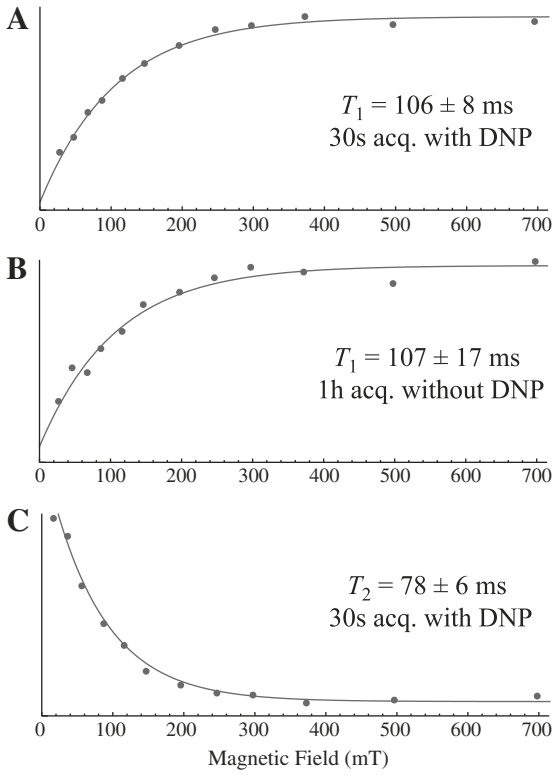

Fig. 5. T_1 measurements (A) with and (B) without DNP and (C) a T_2 measurement with DNP, to illustrate the utility of DNP for relaxation, diffusion or imaging experiments in a low field, portable magnet. The T_2 decay curve does not reach zero due to detection in magnitude mode.

Heisenberg electron exchange must serve to mix many of the transitions, as our results are consistent with the DNP factors calculated when the saturation factor $s^* > 1$. This is important to consider when deciding between the use of low magnetic field or the earth's magnetic field. At first glance, it would seem that the collapse of all hyperfine structure to a single 70 MHz peak at earth's field would be advantageous for saturation, but since Heisenberg spin exchange mixes many of the states, saturation factors s^* at field strengths greater than the earth's magnetic field can be greater than one. The higher theoretical enhancement in the earth's magnetic field is also not a large advantage, as it is outweighed by low thermal polarization. Halse and Callaghan [17] reported a DNP enhancement of −3100 over thermal polarization when saturating at 131.5 MHz and 2.7 mT then detecting at earth's magnetic field, which was convincingly demonstrated to be greater enhancement than possible with prepolarization. Using the Boltzmann distribution, their enhancement value corresponds to an enhanced nuclear polarization of 1.15×10^{-6}. The enhanced polarization at 1.5 mT is about 3 times greater than the DNP-enhanced signal at earth's field, as −350 fold enhancement at 1.5 mT gives a polarization of 3.65×10^{-6}. Given that the earth field setup allows for larger sample volumes than 1.5 mT due to the natural field homogeneity of the earth's magnetic field, the overall signal intensity $\langle I_Z \rangle$ can be comparable. However, the signal to noise ratio (SNR) of DNP-enhanced signal detected at 1.5 mT is still expected to be 380 times larger than DNP-enhanced signal detected at the earth's field, because the SNR of a magnetic resonance experiment increases with proton frequency by a factor of $\omega_H^{3/4}$ in addition to the effect of higher polarization $\langle I_Z \rangle$ [47]. Given the greater detection sensitivity at higher NMR frequencies, the overall SNR of the 1.5 mT system is much higher. A low field system is also less susceptible than an earth's field system to magnetic field inhomogeneities found in the average lab or outdoors near other technical equipment, and thus should be considered when choosing a magnetic field for DNP-enhanced NMR and MRI measurements, even for outdoor and field experiments.

The experiments and conclusions presented here will assist in the selection and optimization of a system to perform DNP-enhanced NMR at low magnetic fields. The frequency of ESR saturation and the concentration of radical both play a large role in determining enhancement, and should be considered when planning a system to perform relaxation measurements, pulsed-field gradient diffusion experiments or acquire images in a low magnetic field.

5. Experimental

All experiments were carried out using a homebuilt DNP apparatus (Fig. 6). The electromagnet was a Helmholtz pair with radii and inter-ring distance of 20.2 cm. Each ring consisted of 138 turns of 15 AWG wire, and a magnetic field of 1.52 mT was produced with a current of 2.500 amps from a GW-Instek PSS-2005 power supply. NMR detection and spectral analysis were performed using an Aurora spectrometer and Prospa software (Magritek Limited, Wellington, New Zealand). A homebuilt solenoid NMR coil with a length of 6.5 cm, diameter of 3.5 cm, and 200 turns of 30 AWG wire was used, and the cable to the coil was equipped with a BLP-1.9 low pass filter (MiniCircuits, Brooklyn, NY, USA). A two turn saddle coil and multiple low pass birdcage coils were constructed for electron excitation. Birdcage coils were built around flat bottom glass tubes 8.5 cm long with a diameter of 2.0 cm and were designed using BirdcageBuilder v1.0 (Penn State College of Medicine, Hershey, PA, USA). The saddle coil was built around a glass tube and was 10 cm long and had a diameter of 2.5 cm. The coils were connected to an LC tuning circuit via coaxial cables and then to a BT00100-AlphaSA-CW amplifier (Tomco Technologies, Norwood, SA, Australia) which was gated by the spectrometer. An HP 8672A Signal Generator (Agilent HP, Santa Clara, CA, USA) was used as a frequency source. A 3 mm thick aluminum box equipped with an air cooling system was used for RF shielding and to cool the sample, and the sample temperature was measured with a thermometer during the experiments. ESR saturation was only applied to the sample during polarization build-up, and was turned off during acquisition and between scans. The NMR coil had a 0.1 ms 90° pulse using an unamplified 8 V transmit voltage and a built-in capacitance of 1 nF.

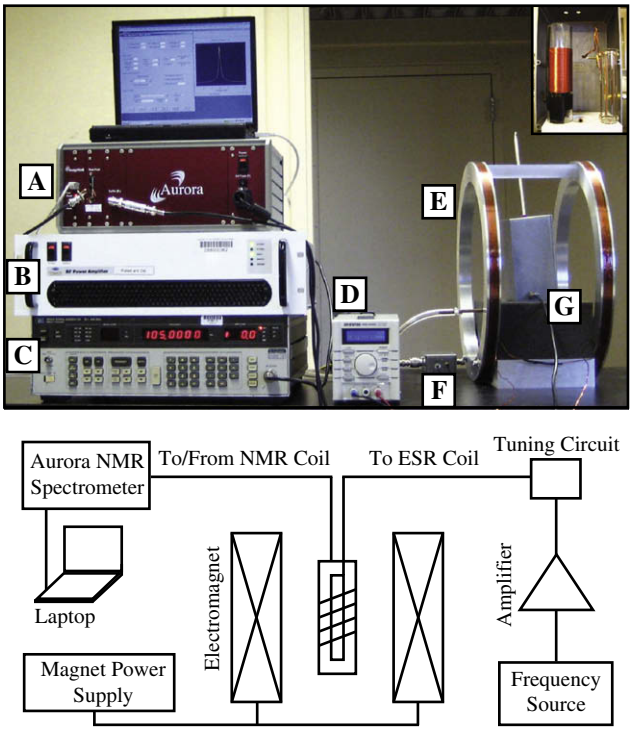

Fig. 6. Photograph and schematic of the DNP-NMR system. Labeled in the photograph are the (A) Aurora NMR spectrometer, (B) Tomco BT00100-AlphaSA-CW amplifier, (C) HP 8672A signal generator, (D) GW-Instek PSS-2005 power supply, (E) electromagnet, (F) homebuilt LC tuning circuit and (G) sample RF shielding box. The inset in the upper right shows inside of the RF shielding box, with the NMR coil on the left and a birdcage coil for ESR saturation on the right. During operation the ESR coil is placed coaxially inside the NMR coil.

4-Amino-2,2,6,6-tetramethylpiperidine-1-oxyl (4-amino-TEMPO 95%) was purchased from Sigma–Aldrich. All samples were prepared by dissolving 4-amino-TEMPO directly in deionized water. The samples were not degassed. 25 mL sample volumes were placed directly into the ESR coils.

For the frequency swept DNP experiment, a birdcage coil, capable of tuning between 70–116 MHz, and a saddle coil, capable of tuning between 9 and 70 MHz were used. ESR irradiation durations of five times the T_1 of the sample were used, followed by the NMR detection pulse. Multiple scans were performed at each point until a good signal was obtained. The resulting NMR peak was used to determine signal enhancement, $\langle I_Z \rangle / I_0$, which was plotted as a function of irradiation frequency. The π transitions were observed by aligning the B_1 field perpendicular to the external magnetic field while the σ transitions were observed with the field parallel to the external field. A low RF power and air cooling were necessary to prevent sample heating. All Plots were created and data was fit with Mathematica 7.0 (Wolfram Research, Champaign, IL, USA). The power output of the birdcage and saddle coils were measured by placing a small pickup coil inside the ESR coil which was connected to an oscilloscope (HP 54110D) by coaxial cable. The peak-to-peak voltage was measured and converted into RMS voltage then B_1 magnitude.

The maximum enhancement was measured using two birdcage coils, one for studying the transitions at 104 and 95 MHz and the other for the 82.5 MHz transition. As in the previous experiment, ESR irradiation durations of five times the T_1 of the sample were used, followed by the NMR detection pulse. The experiment was performed by recording the proton NMR signal enhancement as a function of RF power applied to the amplifier. Sample temperature was maintained within 5 °C of room temperature using airflow of 1.7 cubic meters per hour (60 standard cubic feet per hour) and by varying the length of time between RF irradiation. The E_{max} values were found by using Igor Pro v5.05A (Wavemetrics, Inc., Portland, OR, USA) to fit the data to $E(P) = 1 - AP/(1 + BP)$, where P was power and A and B were free parameters, giving $E_{max} = 1 - A/B$.

The T_1 and T_2 measurements were performed on a 20 mM aqueous solution of 4-amino-TEMPO, and DNP was performed by saturating the T_{16} transition with 104 MHz irradiation. The T_1 was obtained with a standard saturation recovery experiment, with five saturation pulses followed by a variable delay then the 90° pulse and acquisition. The T_2 measurement was performed using a standard 90° – τ – 180° – τ – acquire sequence. With the aid of DNP, only one scan per point was necessary, while without DNP 256 scans/point were used. When the ESR saturation was used a 1s cool down time between experiments was employed.

Acknowledgments

We thank Brandon Armstrong for very helpful discussions of the theory, Craig Eccles and Andrew Coy of Magritek Ltd., for help with our pulse programs and spectrometer, and Bruce Dunson and Terry Hart of the UCSB Chemistry Machine shop for their help with magnet construction. We also thank Megan Halse for discussions of the spectral simulations and help with building the bird cage coils. This work was supported by the Faculty Early CAREER Award (20070057) of the National Science Foundation and the Packard Fellowship for Science and Engineering. A. Cote was supported by the National Nanotechnology Infrastructure Network's Research Experience for Undergraduates program.

References

[1] G. Eidmann, R. Savelsberg, P. Blümler, B. Blümich, The NMR MOUSE, a Mobile Universal Surface Explorer, J. Magn. Reson. A 122 (1996) 104–109.

[2] M.D. Hürlimann, Diffusion and relaxation effects in general stray field NMR experiments, J. Magn. Reson. 148 (2001) 367–378.
[3] A. Mohorič, J. Stepišnik, M. Kos, G. Planinšič, Self-diffusion imaging by spin echo in earth's magnetic field, J. Magn. Reson. 136 (1999) 22–26.
[4] D.G. Rata, F. Casanova, J. Perlo, D.E. Demco, B. Blümich, Self-diffusion measurements by a mobile single-sided NMR sensor with improved magnetic field gradient, J. Magn. Reson. 180 (2006) 229–235.
[5] P.T. Callaghan, C.D. Eccles, T.G. Haskell, P.J. Langhorne, J.D. Seymour, Earth's field NMR in Antarctica: a pulsed gradient spin echo NMR study of restricted diffusion in sea ice, J. Magn. Reson. 133 (1998) 148–154.
[6] M.D. Hürlimann, L. Venkataramanan, Quantitative measurement of two-dimensional distribution functions of diffusion and relaxation in grossly inhomogeneous fields, J. Magn. Reson. 157 (2002) 31–42.
[7] M.E. Halse, A. Coy, R. Dykstra, C. Eccles, M. Hunter, R. Ward, P.T. Callaghan, A practical and flexible implementation of 3D MRI in the Earth's magnetic field, J. Magn. Reson. 182 (2006) 75–83.
[8] K.-J. Dunn, D.J. Berman, G.A. Latorraca, Nuclear Magnetic Resonance Petrophysical and Logging Applications, Pergamon Press, Amsterdam, 2002.
[9] M.J. McCarthy, P.N. Gambhir, A.G. Goloshevsky, NMR for food quality control, in: S. Stapf, S. Han (Eds.), NMR in Chemical Engineering, Wiley-VCH, Weinheim, 2006, pp. 471–490.
[10] H. Van As, T. Scheenen, F. Vergeldt, MRI of intact plants, Photosynth. Res. 102 (2009) 213–222.
[11] B. Blümich, F. Casanova, Mobile NMR, in: G.A. Webb (Ed.), Modern Magnetic Resonance, Springer, Dordrecht, 2006, pp. 373–382.
[12] M. Brai, M. Camaiti, C. Casieri, F. De Luca, P. Fantazzini, Nuclear magnetic resonance for cultural heritage, Magn. Reson. Imaging 25 (2007) 461–465.
[13] B. Blümich, J. Perlo, F. Casanova, Mobile single-sided NMR, Prog. Nucl. Magn. Reson. Spectrosc. 52 (2008) 197–269.
[14] M. Packard, R. Varian, Free nuclear induction in the earths magnetic field, Phys. Rev. 93 (1954) 941.
[15] W. Shao, G. Wang, R. Fuzesy, E.W. Hughes, B.A. Chronik, G.C. Scott, S.M. Conolly, A. Macovski, Low readout field magnetic resonance imaging of hyperpolarized xenon and water in a single system, Appl. Phys. Lett. 80 (2002) 2032–2034.
[16] T. Guiberteau, D. Grucker, EPR spectroscopy by dynamic nuclear polarization in low magnetic field, J. Magn. Reson. B 110 (1996) 47–54.
[17] M.E. Halse, P.T. Callaghan, A dynamic nuclear polarization strategy for multi-dimensional Earth's field NMR spectroscopy, J. Magn. Reson. 195 (2008) 162–168.
[18] C. Polyon, D.J. Lurie, W. Youngdee, C. Thomas, I. Thomas, Field-cycled dynamic nuclear polarization (FC-DNP) of ^{14}N and ^{15}N nitroxide radicals at low magnetic field, J. Phys. D 40 (2007) 5527–5532.
[19] C.R. Bowers, D.P. Weitekamp, Parahydrogen and synthesis allow dramatically enhanced nuclear alignment, J. Am. Chem. Soc. 109 (1987) 5541–5542.
[20] T.C. Eisenschmid, R.U. Kirss, P.P. Deutsch, S.I. Hommeltoft, R. Eisenberg, J. Bargon, R.G. Lawler, A.L. Balch, Para hydrogen induced polarization in hydrogenation reactions, J. Am. Chem. Soc. 109 (1987) 8089–8091.
[21] J.H. Ardenkjaer-Larsen, B. Fridlund, A. Gram, G. Hansson, L. Hansson, M.H. Lerche, R. Servin, M. Thaning, K. Golman, Increase in signal-to-noise ratio of >10,000 times in liquid-state NMR, Proc. Nat. Acad. Sci. USA 100 (2003) 10158–10163.
[22] D. Grucker, *In vivo* detection of injected free radicals by Overhauser effect imaging, Magn. Reson. Med. 14 (1990) 140–147.
[23] D.J. Lurie, G.R. Davies, M.A. Foster, J.M.S. Hutchison, Field-cycled PEDRI imaging of free radicals with detection at 450 mT, Magn. Reson. Imaging 23 (2005) 175–181.
[24] D.J. Lurie, K. Mäder, Monitoring drug delivery processes by EPR and related techniques–principles and applications, Adv. Drug Deliv. Rev. 57 (2005) 1171–1190.
[25] D. Grucker, Oxymetry by magnetic resonance: applications to animal biology and medicine, Prog. Nucl. Magn. Reson. Spectrosc. 36 (2000) 241–270.
[26] D. Grucker, J. Chambron, Oxygen imaging in perfused hearts by dynamic nuclear polarization, Magn. Reson. Imaging 11 (1993) 691–696.
[27] T. Guiberteau, D. Grucker, Dynamic nuclear polarization imaging in very low magnetic fields as a noninvasive technique for oximetry, J. Magn. Reson. 124 (1997) 263–266.
[28] D.I. Potapenko, M.A. Foster, D.J. Lurie, I.A. Kirilyuk, J.M.S. Hutchison, I.A. Grigor'ev, E.G. Bagryanskaya, V.V. Khramtsov, Real-time monitoring of drug-induced changes in the stomach acidity of living rats using improved pH-sensitive nitroxides and low-field EPR techniques, J. Magn. Reson. 182 (2006) 1–11.
[29] G.S. Ananchenko, E.G. Bagryanskaya, R.Z. Sagdeev, Low magnetic field electron-nuclear resonance transitions detected by nuclear polarization of radical reaction products, Chem. Phys. Lett. 282 (1998) 450–455.
[30] N. Kernevez, H. Glenat, Description of a high-sensitivity CW scalar DNP-NMR magnetometer, IEEE Trans. Magn. 27 (1991) 5402–5404.
[31] A.M.F. Benial, K. Ichikawa, R. Murugesan, K.-i. Yamada, H. Utsumi, Dynamic nuclear polarization properties of nitroxyl radicals used in Overhauser-enhanced MRI for simultaneous molecular imaging, J. Magn. Reson. 182 (2006) 273–282.
[32] T. Guiberteau, D. Grucker, Dynamic nuclear polarization of water protons by saturation of σ and π EPR transitions of nitroxides, J. Magn. Reson. A 105 (1993) 98–103.
[33] D. Grucker, T. Guiberteau, B. Eclancher, J. Chambron, R. Chiarelli, A. Rassat, G. Subra, B. Gallez, Dynamic nuclear polarization with nitroxides dissolved in biological fluids, J. Magn. Reson. B 106 (1995) 101–109.
[34] D.J. Lurie, I. Nicholson, J.R. Mallard, Low-field EPR measurements by field-cycled dynamic nuclear polarization, J. Magn. Reson. 95 (1991) 405–409.
[35] A.O. Salman, M.M. Sünnetçioglu, R. Sungur, G. Bingöl, A DNP investigation of π and σ transitions for nitroxide spin probes at 1.53 mT, J. Magn. Reson. 134 (1998) 1–6.
[36] I. Sert, M.M. Sunnetcioglu, R. Sungur, G. Bingol, Dynamic nuclear polarization studies of TANOL/water–glycerol solutions, Z. Naturforsch. A 55 (2000) 682–686.
[37] V.W. Müller-Warmuth, Untersuchungen zur protonenpolarisation durch Overhauser-effekt und zur paramagnetischen relaxation in $(SO_3)_2NO$–lösungen, Z. Naturforsch. 15a (1960) 927–939.
[38] M. Fedin, S. Shakirov, P. Purtov, E. Bagryanskaya, Electron spin relaxation of radicals in weak magnetic fields, Russ. Chem. Bull. 55 (2006) 1703–1716.
[39] G. Breit, I.I. Rabi, Measurement of nuclear spin, Phys. Rev. 38 (1931) 2082.
[40] B. Borah, R.G. Bryant, NMR relaxation dispersion in an aqueous nitroxide system, J. Chem. Phys. 75 (1981) 3297–3300.
[41] K.H. Hausser, D. Stehlik, Dynamic nuclear polarization in liquids, Adv. Magn. Reson. 3 (1968) 79–139.
[42] B.D. Armstrong, S. Han, A new model for Overhauser enhanced nuclear magnetic resonance using nitroxide radicals, J. Chem. Phys. 127 (2007) 104508.
[43] J.P. Lloyd, G.E. Pake, Spin relaxation in free radical solutions exhibiting hyperfine structure, Phys. Rev. 94 (1954) 579.
[44] J.A. Weil, J.R. Bolton, J.E. Wertz, Electron Paramagnetic Resonance: Elementary Theory and Practical Applications, Wiley, New York, 1994.
[45] J.R.D. Bates, W.S. Drozdoski, Use of nitroxide spin labels in studies of solvent–solute interactions, J. Chem. Phys. 67 (1977) 4038–4044.
[46] R.D. Bates, Polarization of solvent nuclei by nitroxide spin labels at low magnetic fields, J. Magn. Reson. 48 (1982) 111–124.
[47] D.I. Hoult, R.E. Richards, The signal-to-noise ratio of the nuclear magnetic resonance experiment, J. Magn. Reson. 24 (1976) 71–85.